

ARTICLES

The Size-Dependent Structural Phase Behaviors of Supported Bimetallic (Pt–Ru) Nanoparticles

Charles W. Hills, Nathan H. Mack, and Ralph G. Nuzzo*

*School of Chemical Sciences and the Frederick Seitz Materials Research Laboratory, University of Illinois, Urbana, Illinois 61801**Received: October 4, 2002; In Final Form: December 17, 2002*

We describe in this report the preparation, structural characterization, and phase behaviors exhibited by supported metallic and bimetallic nanoparticles. Homometallic nanoparticles of either Pt or Ru were synthesized by the reduction of various precursors ($(\text{CH}_3)_2\text{Pt}(\text{COD})$, H_2PtCl_6 , and RuCl_3) onto different carbon supports: Vulcan XC-72 (VXC) and Shawinigan Acetylene Black (SAB). The choice of precursor has a large structural influence on the reductive condensation of the Pt metal particles. All of the various precursors and supports produced particles with very similar size distributions, with the exception of $(\text{CH}_3)_2\text{Pt}(\text{COD})$, which formed a complex distribution of small (20 Å) and large (>50 Å) particles. The centerpiece of this study is the characterization of the growth behaviors seen in the synthesis of binary Pt–Ru nanoparticles. These heterometallic particles were synthesized via a seeded reductive condensation of one metal precursor onto pre-supported nanoparticles of a second metal; the latter serve as nucleating sites for the growth of the binary phase. As shown via data from X-ray photoelectron spectroscopy (XPS), electron microscopy, and energy-dispersive X-ray analysis (EDX), this growth technique yields fully alloyed metallic nanoparticles, albeit ones of varying size and compositional distributions depending on the specific conditions used. Generally we found that the particles had a wide composition distribution. The nature of this distribution and the correlations between the nanoparticle sizes, compositions, and structures embedded in it were characterized in depth by scanning transmission electron microscopy (STEM). These results are used to establish an apparent size correlated binary phase diagram of the bimetallic (Pt–Ru) nanoparticles. The structural properties of the supported bimetallic nanoclusters are different from that of the bulk, as evidenced by the presence of strongly persistent metastable structures that are not found in the bulk phase diagram.

Introduction

Nanometer-sized metal particles are of great interest in current research due in no small part to the unique physical and chemical properties they exhibit.^{1–9} These materials find uses in areas as diverse as microelectronics, optics, and industrial catalysis.^{1–9} Frequently, the properties exhibited by metal clusters in such applications depend strongly on perturbations that arise from the large fraction of metal atoms that reside at the particle surface.^{1–9} There arises from this fact a rich range of structural chemistries that produce striking differences between the properties found in the bulk when compared to those of a nanoscale system. The current research addresses itself to this interest, seeking to develop a better understanding of the structure and reactivity of metallic nanoparticles with useful applications in technology.

In this present report, we consider the structural properties of binary nanoparticles, ones grown using a growth strategy that serves to decouple particle growth from particle nucleation by seeding the reaction with previously produced supported homometallic nanoparticles (Scheme 1). In this synthesis, a

SCHEME 1



precursor for one of the constituent metals is impregnated onto a carbon support bearing existing metal nanoclusters of the other component. The nascent cluster nuclei are added to the reaction mixture at a level sufficient to yield a desired binary composition via the reductive condensation of a second homometallic precursor on these centers. The data show that the clusters do in fact serve as nucleation centers for the growth of binary phases. The structure of the materials obtained via this process were fully characterized in studies emphasizing the application of high-resolution scanning transmission electron microscopy (STEM).

Carbon-supported Pt–Ru alloy nanoparticles have attracted interest in research due to their superior activity as anode catalysts for methanol electrooxidation.¹⁰ The marked improvements they yield over pure Pt nanoparticles notably include an ability to better resist poisoning by CO.¹⁰ These improvements, however, have yet to relieve the need for more active electro-

* Corresponding author. Tel.: (217) 244-0809. Fax: (217) 244-2278. E-mail: r-nuzzo@uiuc.edu.

catalyst materials for use in commercially viable polymer electrolyte fuel cells, most notably direct methanol fuel cells (DMFC).^{10–13} There further exists a significant need in DMFC technologies to improve the usage of noble metal loadings, especially for the cell anode.¹⁰ Supported catalysts are therefore of interest in this regard. Carbon is a natural choice for a support phase since it also has the requisite property of being able to serve as a current collector. To improve the performance realized by devices using supported alloy catalysts, it remains a critical need in research to define a comprehensive set of rate–structure correlations to guide their development. The literature on this topic, in particular as related to the structural habits of supported Pt–Ru alloy phases^{14,15} and the phase dynamics of nanoscale materials more generally,^{14–17} remains limited at best.

Much of the current understanding of the mechanisms involved in methanol oxidation with Pt–Ru electrocatalysts is based on studies using well-defined planar-polycrystalline Pt–Ru electrodes,^{10–13} or on model cell assemblies containing significant loadings of metal alloy catalysts.^{10–13,18} To bridge these results to a detailed understanding of the structural dependencies of the electrocatalytic reaction rates realized over nanometer-sized supported bimetallic particles will require significant new insights into the structural properties of these systems.^{10,13,14,19–21} It is to this latter interest that this research is addressed.

It is well-known that nanoscale materials often have different chemical and physical properties than those that characterize similar compositions in the bulk.^{1–9} The finite size of nanoscale materials frequently leads to perturbations that result in new (i.e., nonbulk-like) behaviors.² Quantum confinement in semiconductor nanoparticles is a well-known example that has received considerable attention in research and lies at the heart of a number of useful electronic and optical properties.^{3,6,7} It is only more recently, however, that the complex nature of the structural and chemical properties of nanoscale materials have become the focus of detailed, atomistic level studies.^{1–3,6,7,19–22} A result from our past work, for example, showed that bimetallic (Pt–Ru) nanoparticles (~1.5 nm diameter) synthesized from molecular precursors with a 1:5 Pt:Ru ratio assume a face-centered cubic (fcc) closest-packed structure.¹⁹ This observation is intriguing, since a bulk alloy of this composition (ca. 85% Ru) would assume a hexagonal-closest packed (hcp) structure.²³ This simple data point suggests that an interesting divergence may exist between the structural properties predicted by the bulk binary phase diagram and those exhibited by very small supported clusters. Extending this understanding to fully develop the relationships that exist between composition, size, and ultimately the structure adopted, could provide critical new insights into the features that lead to the useful catalytic activities of metallic nanoparticles.

To accomplish the detailed structural characterizations reported in this work, we take advantage of the significant improvements that have been made in analytical techniques for characterizing nanoscale materials.^{24–31} Electron microscopy, most notably scanning transmission electron microscopy (STEM), is an extremely useful tool for characterizing small metal particles. Current instruments can examine supported metal nanoparticles with essentially atomic resolution.^{29–31} In addition, the flexible electron-optical systems of modern microscopes allow the collection of electron diffraction patterns from single clusters present in a selected image field.^{24–28} Combining the imaging power of scanning transmission electron microscopes with the microcharacterization data gathered from energy-dispersive X-ray analysis (a correlated electron probe method

with the ability to analyze composition at the single-particle level),^{29,30} a complete picture of the final nanoparticle “phase-sensitive” structure can be obtained.

In this study, we report on the synthesis of both homometallic and heterometallic nanoparticles of Pt, Ru, and Pt–Ru. Using a battery of analytical tools, including X-ray photoelectron spectroscopy (XPS), scanning transmission electron microscopy (STEM), energy-dispersive X-ray analysis (EDX), and electron nanodiffraction, we characterize the size distributions, compositions, and microstructures of the particles. By using several precursors, supports, and further examining alloying reactions carried out on supports bearing extant monometallic clusters, it is possible to probe the effect that each has on the cluster assembly and growth processes. Each of these nanoscale material systems is structurally characterized at the single-particle level using the electron beam probe methods. Correlating these latter data by size and composition, we deduce an apparent binary nanophase diagram for the bimetallic particles. These data suggest that the supported clusters can exhibit significant metastability. Even so, the systems clearly reveal a tendency for Pt–Ru binary phases of any composition at sizes near 2 nm in diameter to prefer the adoption of fcc habits.

Experimental Section

Materials. The $\text{RuCl}_3 \cdot x\text{H}_2\text{O}$ (further referred to as RuCl_3), $(\text{CH}_3)_2\text{Pt}(\text{COD})$ (where COD is 1,5-cyclooctadiene), and $\text{H}_2\text{PtCl}_6 \cdot 6\text{H}_2\text{O}$ (further referred to as H_2PtCl_6) were purchased from STREM Chemicals. Reagent grade tetrahydrofuran (THF) was obtained from Aldrich Chemicals. Supported platinum and ruthenium particles (10 wt % on VXC) were obtained from E-TEK, Inc. VXC was supplied by Cabot, while SAB (50% compressed) was obtained from Chevron.

Sample Preparation. Solutions of RuCl_3 , $(\text{CH}_3)_2\text{Pt}(\text{COD})$, and H_2PtCl_6 were made by dissolving each in tetrahydrofuran, followed by sonication to ensure complete dissolution. To deposit Ru onto commercial samples of supported Pt particles (Ru:Pt/C), the supported Pt particles (E-TEK, Inc.) were added to a RuCl_3 solution, sonicated, and then dried under a stream of N_2 . To ensure homogeneity, the cycle of THF addition, sonication, and drying was repeated a total of three times. The same process was followed for the deposition of Pt onto commercial samples of Ru particles (Pt:Ru/C), except carbon-supported Ru particles (E-TEK, Inc.) were added to a solution of either $(\text{CH}_3)_2\text{Pt}(\text{COD})$ or H_2PtCl_6 . Monometallic nanoparticles were prepared by incorporating each of the three precursors onto the carbon supports (VXC and SAB) using the same method described above.

After incorporating the metallic salts, reduction was accomplished by placing the samples in a custom tube furnace under a constant flow of H_2 . The temperature was then ramped to 673 K over a period of several hours, held there for 1 h, and then allowed to cool under an H_2 purge. In addition, a sample of Ru on Pt was also reduced at a higher temperature, 823 K, to examine the affect of temperature on the final structural states of the particles.

X-ray Photoelectron Spectroscopy (XPS). XPS data for the supported nanoparticles were collected using a Perkin-Elmer/PHI XPS 5400 spectrometer with either Mg K_α (15 kV, 400 W) or Al K_α (15 kV, 400 W) radiation. To reduce damage to the unreduced samples, monochromatic Al K_α radiation was used to follow the reduction. The data were collected at a sample tilt angle of 45° and analyzed using a hemispherical analyzer. The samples were prepared by pressing the powdered carbon-supported samples onto double-sided copper tape.

Scanning Transmission Electron Microscopy. Microscopy studies were performed using a field emission Vacuum Generators HB-501 scanning transmission electron microscope operated at 100 kV. The specimens were prepared by dipping copper-supported holey carbon grids (SPI supplies) into the previously reduced powdered samples. Image analysis was performed using Digital-micrograph (GATAN) digital-video data-acquisition software. The particle sizes were determined by measuring the full width at half-maximum of the cross-section intensity profiles of individual nanoparticles along the longest axis.

The composition of the selected nanoparticles was determined by energy-dispersive X-ray (EDX) analysis. In this analysis, the incident probe beam was located on a single particle and the X-ray fluorescence detected. EDX data acquisition and analysis were carried out using Link ISIS (Oxford) software, and the quantitative analyses were based on the characteristic X-ray fluorescence lines of Pt and Ru (Ru $L_{\alpha\beta}$ 2.6 keV; Ru L_{γ} 3.2 keV; Ru K_{α} 19.2 keV; Pt $M_{\alpha\beta}$ 2.1 keV; Pt L_{α} 9.4 keV; Pt L_{α} 11.1 keV; Pt L_{β} 11.3 keV).

The ordered microstructure of the nanoparticles was probed by electron nanodiffraction. The specimens were prepared in a manner similar to those for the microscopy study, except copper mesh, holey carbon grids (SPI supplies) with silicon crystals (in-house procedure) were used to support the samples. An incident electron beam probe was focused on the nanoparticles of interest, and the diffracted electrons were collected on a phosphor screen. Due to the fact that the diffraction patterns for individual nanoparticles degrade during exposure to the electron beam, the diffraction images were gathered promptly. A low-light level television camera was used to this end and Scion Image (NIH/Scion Corp.) software used to capture the images. Digital Microscopist (Virtual Laboratories) software was then used to analyze the patterns, using diffraction patterns from the silicon crystals to calibrate the camera constant.

Results

X-ray Photoelectron Spectroscopy. Figure 1, A and B, show representative survey spectra taken before and after reduction that document the formation of Pt nanoparticle samples using H_2PtCl_6 as a precursor. The sample examined here corresponds to ca. 20 wt % loading of Pt on a SAB support. As can be seen, the unreduced spectrum has a clear Cl-2p peak at ca. 200 eV. Figure 1C shows the Pt-4f region of the unreduced sample, while Figure 1D displays the same region of the reduced nanoparticles. The dashed line in both samples coincides with the Pt-4f_{7/2} binding energy in the reduced sample, which is consistent with metallic Pt.³² There is roughly a 2 eV shift in the unreduced sample, which is consistent with a Pt(IV)-halide species.³²

Data provided in the Supporting Information gives insights into the analogous formation of homometallic Ru and Pt nanoparticles made from $RuCl_3$ and $(CH_3)_2Pt(COD)$, respectively. These data reveal that there is roughly a ~1.3 eV shift of the Ru-3p_{3/2} core-level peak toward lower binding energy and the loss of all intensity for the Cl-1s peak after reduction, which indicates the complete reduction of the Ru(III) species to Ru metal.³² The $(CH_3)_2Pt(COD)$ sample shows a similar reduction-induced shift in the Pt-4f_{1/2} peak; however, there is an interesting feature of the unreduced sample not present in other samples. These data specifically suggest that some of the Pt precursor in this instance spontaneously decomposes to give a mixture of higher valent and lower valent (possibly Pt(0)) species. The high binding energy of the second Pt component could be indicative of disproportionation processes being involved. Such assignments remain tenuous at best, given the

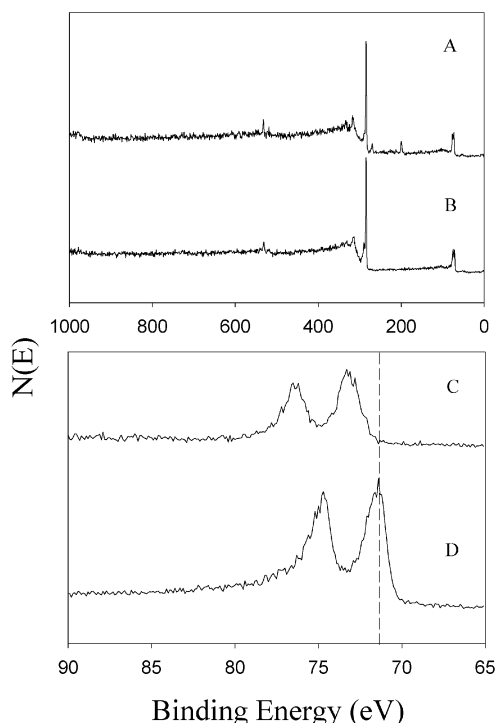


Figure 1. XPS spectra of reduced and unreduced 20% Pt supported on SAB from H_2PtCl_6 : (A) Unreduced survey data; (B) Reduced survey data; (C) Unreduced Pt-4f region; (D) Reduced Pt-4f region.

uncertainty that surrounds our understanding of the species present and the contributions that final state effects would make to their binding energies.

Taken together, the data presented in Figure 1 and the Supporting Information illustrate that the incubation of the various carbon supports with any of the reagent complexes, when followed by a high-temperature treatment in H_2 , leads to the formation of metallic particles. The ligands, at least for the case of Cl, are not retained, apparently being lost to the gas phase (most likely as HCl).

Figure 2 shows XPS data following the reduction of $RuCl_3$ (Ru) dispersed on a carbon support (VXC) bearing preformed metallic Pt nanoparticles (Pt/C), a reaction that leads to the formation of bimetallic nanoparticles (Ru:Pt/C). Figure 2, A and B, present survey spectra for samples of 10% Pt/C measured both before and after the addition and subsequent reduction of the $RuCl_3$ precursor. The strong signal seen in the Pt-4f region (~70 eV) arises as a result of the small metallic Pt clusters that are present in the Pt/C sample. The addition of the Ru precursor, upon reduction, leads to the formation of metallic Ru species. This is best seen by considering the Ru-3p_{3/2} core level data shown in Figure 2, C and D. In the pure 10% Pt/C sample, there is no peak seen in this region; however, after addition and reduction of the Ru salt a 3p_{3/2} core level is seen that is consistent with the presence of Ru(0). A quantitative analysis of the XPS core level data suggests that an average Ru-to-Pt composition of 1.09:1 is present in this sample. This compares well to the 1:1 ratio expected on the basis of the formal stoichiometry of the $RuCl_3$ and Pt/C used to generate this sample. The presence of alloys, though, can only be established by direct microanalytical measurements such as are afforded by STEM (see below).

Related sets of XPS data that characterize the formation of bimetallic Pt:Ru/C nanoparticles (particles formed from the reduction of either a H_2PtCl_6 or $(CH_3)_2Pt(COD)$ precursor (Pt) onto preformed carbon-supported (VXC) Ru particles (Ru/C))

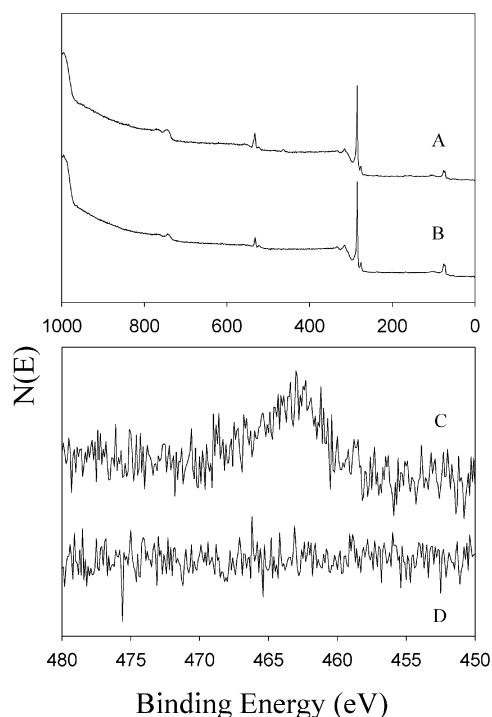


Figure 2. XPS spectra for bimetallic Pt–Ru nanoparticles with a 1:1 atomic ratio, made from 10% Pt/C + RuCl₃: (A) Survey data of the Pt/C + RuCl₃ particles after reduction; (B) Survey data of the Pt/C particles before the addition of RuCl₃; (C) Ru-3p region of the Pt/C + RuCl₃ particles after reduction; (D) Ru-3p region of the Pt/C particles before the addition of RuCl₃.

are included in the Supporting Information. The core level data in both instances reveal the presence of metallic Pt and Ru species. A quantitative analysis of the Pt and Ru core level intensities again proves instructive. The sample derived from H₂PtCl₆ showed an average Pt-to-Ru composition of 1.4:1, while that from (CH₃)₂Pt(COD) was 1.1:1. The value for the (CH₃)₂Pt(COD)-derived sample correlates reasonably to the 1:1 stoichiometry expected. The H₂PtCl₆-derived sample, however, does not. The XPS measurement, in this case may in fact be illustrating the effects of heterogeneity that may be present in the sample. Since XPS is a surface-sensitive technique, segregation effects or inhomogeneous distributions of species within the support could lead to results that deviate significantly from the true average compositions present. For this reason, these data should be considered in this context with some caution. Electron-probe microscopies, however, do speak very directly to this latter type of analysis. It is to such studies that we now turn our attention.

Scanning Transmission Electron Microscopy. Figure 3 shows representative dark-field micrographs of 10% Ru/C-supported nanoparticles and bimetallic alloy clusters (Pt:Ru/C) grown using this material as a promoted substrate. The two Pt precursors used were as before, H₂PtCl₆ (Figure 3B) and (CH₃)₂Pt(COD) (Figure 3C), and combined so as to give a 1:1 stoichiometry of the metals. Figure 4 shows the corresponding particle size distributions measured for these samples. The average size of the starting Ru/C particles measured for this commercial 10% loading sample (Figure 4A) was ~25 Å. Addition of the Pt precursors, after a subsequent reduction, shifts and broadens the particle size distributions (Figures 4B and C) as expected toward larger values. The population of the cluster sizes seen is notably asymmetric toward the larger diameters. The trends in qualitative terms are consistent with the condensation of Pt atoms onto the supported Ru particles, suggesting

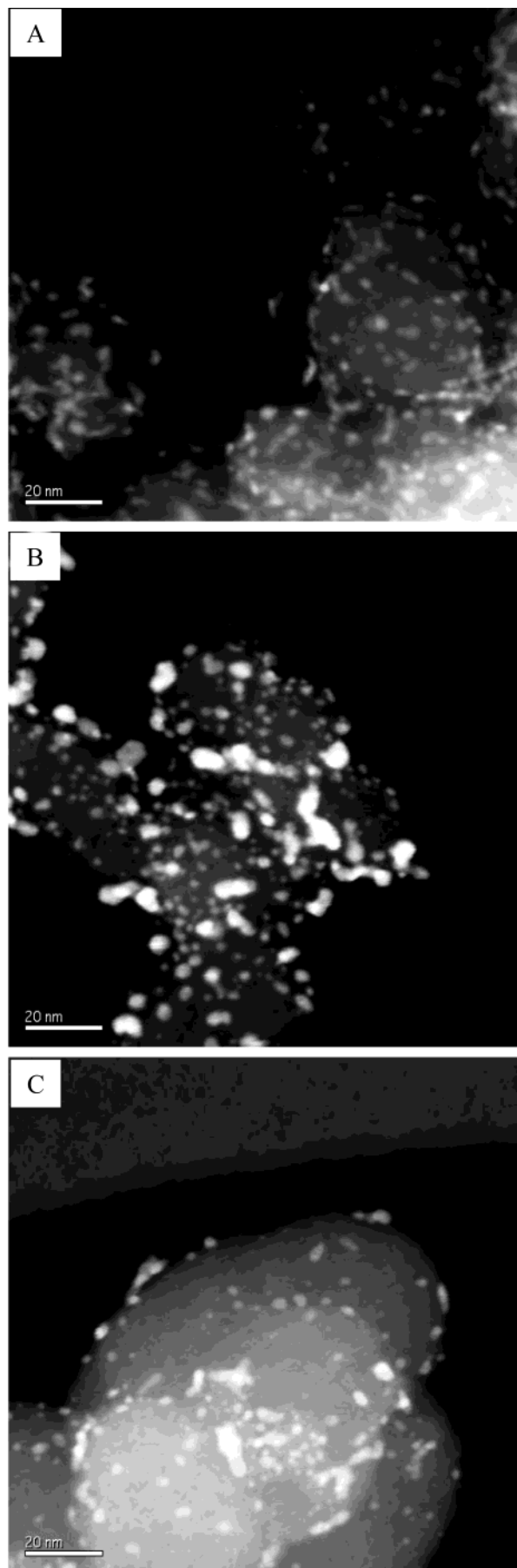


Figure 3. Representative dark-field micrographs of (A) 10% Ru/C; (B) 10% Ru/C + H₂PtCl₆ after reduction; and (C) 10% Ru/C + (CH₃)₂Pt(COD) after reduction.

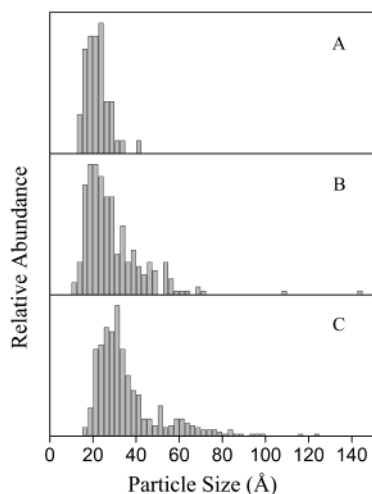


Figure 4. Particle size distribution for (A) 10% Ru/C; (B) 10% Ru/C + H_2PtCl_6 after reduction; and (C) 10% Ru/C + $(\text{CH}_3)_2\text{Pt}(\text{COD})$ after reduction.

that the latter may serve to nucleate the reductive growth of the Pt to some degree. Figures 5 and 6 provide a similar analysis for bimetallic (Ru:Pt/C) nanoparticles grown using nascent Pt clusters to nucleate the reductive condensation of the heterometallic atoms from RuCl_3 . Again, the materials were combined so as to give a 1:1 stoichiometry of Pt to Ru. The starting Pt/C sample bears Pt nanoparticles that have an average particle size of ~ 20 Å (Figure 6A). Reaction of these clusters with RuCl_3 shifts and broadens the distribution to values lying well above 30 Å (Figure 6B). Increasing the reduction temperature from 673 K to 823 K (Figure 6C) had little effect on the final particle size distribution. The starting commercial Ru/C and Pt/C particles (Figures 3A and 5A, respectively) show relatively narrow size distributions. An important feature to note in the larger set of data, one common to the nucleated growth method used to prepare the bimetallic samples, is that the promoted alloy synthesis always generates product distributions that are broader than those of the starting supported clusters. We defer further discussion of this until later.

We should note that the clusters used to nucleate the binary phase nanoparticles do influence the characteristics of the size distributions obtained. This is best illustrated by the nature of the cluster structures obtained from a similar precursor reduction carried out in the absence of a nucleating cluster. Representative dark-field micrographs for Pt and Ru monometallic samples obtained in this way are included in the Supporting Information. Nanoparticles produced via the reduction of the various homometallic precursors show some sensitivity to the choice of support, as illustrated by a quantitative analysis made in terms of the representative distributions of the particle sizes present. Generally speaking, a 20 metal-weight-percent loading of the precursors gave clusters with an average dimension centered near 5 nm, with one notable exception being the Pt clusters formed on the SAB carbon support using the $(\text{CH}_3)_2\text{Pt}(\text{COD})$ precursor. On average, these latter particles were more than 20 Å larger than those obtained using any of the precursors on the other carbon support. For this reason, we restricted our attention to VXC-supported materials in studies of bimetallic particles.

The monometallic particle data also reveals one somewhat more subtle point of interest related to the particle growth seen in the Pt samples. On average, the particles formed from any precursor were always bigger on SAB carbons, with those derived from $(\text{CH}_3)_2\text{Pt}(\text{COD})$ always being larger than those formed from H_2PtCl_6 . This size difference is smaller in the

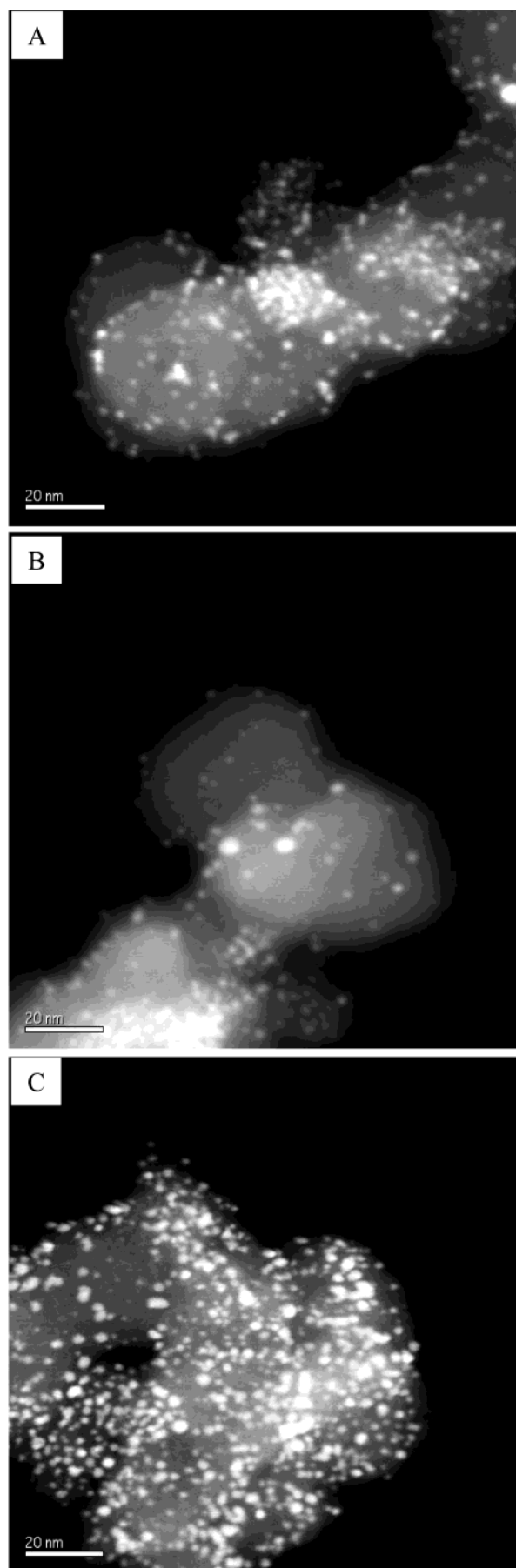


Figure 5. Representative dark-field micrographs of (A) 10% Pt/C; (B) 10% Pt/C + RuCl_3 after reduction at 673 K; and (C) 10% Pt/C + RuCl_3 after reduction at 823 K.

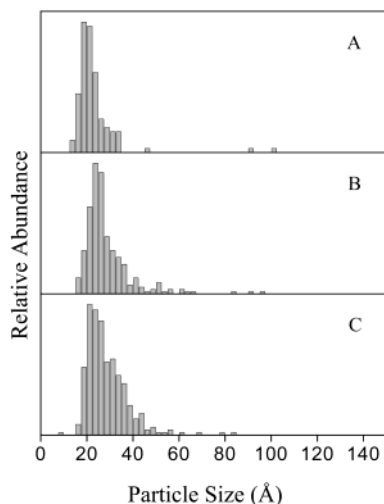


Figure 6. Particle size distribution for (A) 10% Pt/C; (B) 10% Pt/C + RuCl₃ after reduction at 673 K; and (C) 10% Pt/C + RuCl₃ after reduction at 823 K.

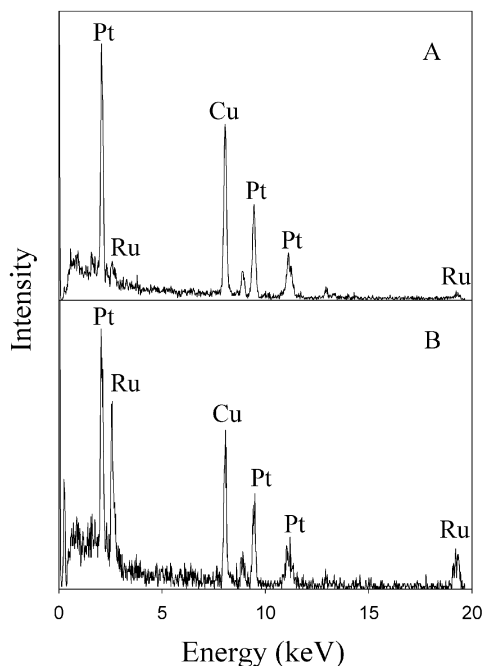


Figure 7. Representative EDX spectra of (A) a particle with 15% Ru; and (B) a particle with 60% Ru.

VXC-supported samples, but still it remains a structural trend evidenced on both carbon supports.

The compositions of the nanoparticles within the image field were determined by energy-dispersive X-ray (EDX) analyses. Figure 7 shows representative EDX spectra collected for 2 particles with different Pt–Ru ratios (15% and 60% Pt) and strikingly illustrates the sensitivity of this microanalytical method (the Cu signal is a diffuse background from the grid used to hold the sample). Figure 8 shows the representative composition distributions derived from numerous individual EDX spectra like those shown in Figure 7. Figure 8, A–C, represent the individual data sets measured for the three different bimetallic samples (RuCl₃ on Pt/C, (CH₃)₂Pt(COD) on Ru/C, and H₂PtCl₆ on Ru/C). The averages are not precisely weighted, at least not apparently so, at the expected 1:1 composition. We note that these data do not directly correlate with the distributions of mass present since the sizes of the particles are not accounted for in this figure. The significant point to take away

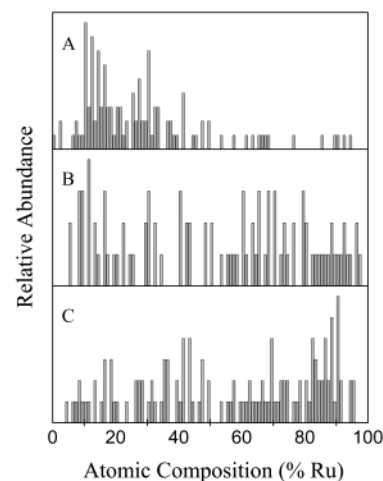


Figure 8. Compositional distribution of bimetallic nanoparticles: (A) 10% Pt/C + RuCl₃; (B) 10% Ru/C + H₂PtCl₆; (C) 10% Ru/C + (CH₃)₂Pt(COD). The smallest bar in the plot represents one particle count.

from these data is that the seeded growth process leads to the formation of nanoparticles with a wide range of compositions (0–100% Ru). This compositional heterogeneity is obtained irrespective of whether the Pt is grown on a Ru core cluster or vice versa. The ability of the microscopy to analyze structure at the limit of individual bimetallic nanoparticles allows us to examine ensemble properties of this system in a very deep way. We turn now to a consideration of the apparent phase dynamics revealed by a correlation of these data with microdiffraction studies. Of central interest in this regard is the development of an understanding of whether the final nanocluster's composition dependent structure results from thermodynamic control or if in fact metastable (i.e., kinetic) structures are also important.

The nanoparticle structures were established by electron nanodiffraction.^{24–28} Strong electron diffraction is seen from all the nanocrystal samples examined in this work; representative patterns are shown in the figures provided in the Supporting Information section. Comprehensive tabulations of the size and composition dependencies of the nanodiffraction data are shown in Figure 9. Superimposed on these plots are the stability limits found in the bulk phase diagram (dashed lines).

The Pt:Ru bulk phase diagram exhibits a wide miscibility gap, with fcc and hcp structures present at high and low Pt concentrations, respectively. The composition-dependent structures seen in the size-correlated diagrams (constructs that can be analyzed as to their predictive qualities of nanoparticle structure) differ frequently from that predicted by the bulk phase diagram.²³ The data shown in Figure 9(A–C) correspond to samples formed on VXC using either Pt/C (Figure 9A) or Ru/C (Figure 9, B and C) supports to nucleate the particle growth. The Pt samples (Figure 9, B and C) were grown using H₂PtCl₆ and (CH₃)₂Pt(COD) as the precursors, respectively. The data in Figure 9D are a summary of all the data points given in Figure 9(A–C). To test for any temperature dependent structural effects, a sample (Ru:Pt/C) was reduced at an elevated temperature and similarly analyzed, these data are given in the Supporting Information section. The nanophase diagrams in each case clearly show a dominant preference for fcc structures in this size range at essentially all but the most Ru-rich compositions when the particles are made using this growth strategy (Scheme 1).

As a control, a mixture of H₂PtCl₆ and RuCl₃ were simultaneously reduced in the presence of VXC (i.e., no unsupported particles are initially present). The nanoparticles produced by

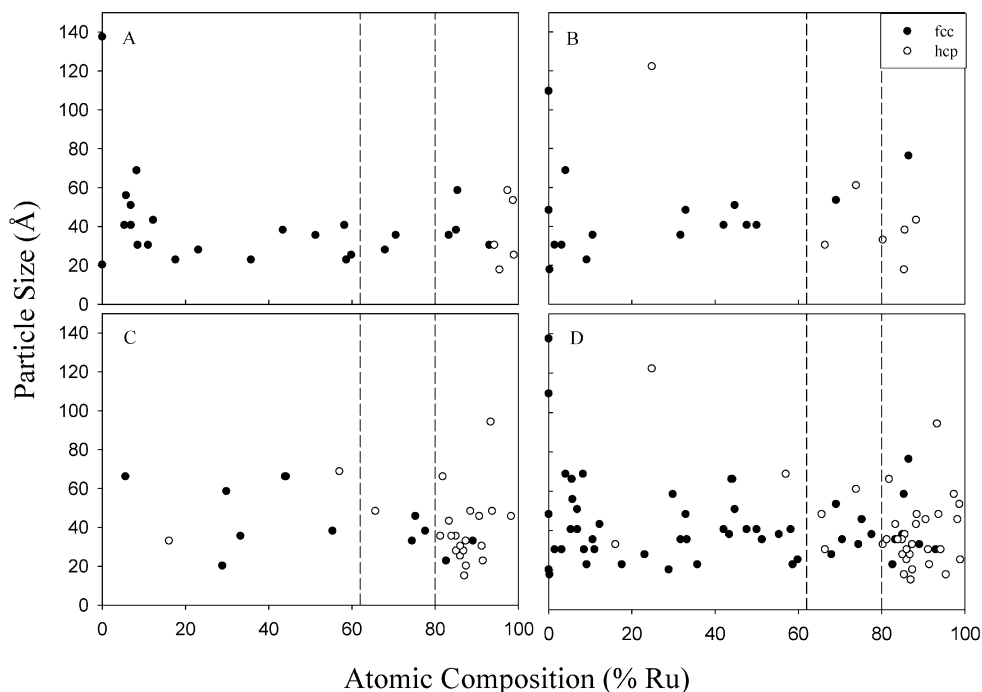


Figure 9. Phase diagrams of bimetallic nanoparticles: (A) 10% Pt/C + RuCl_3 ; (B) 10% Ru/C + H_2PtCl_6 ; (C) 10% Ru/C + $(\text{CH}_3)_2\text{Pt}(\text{COD})$; (D) sum of A, B, and C.

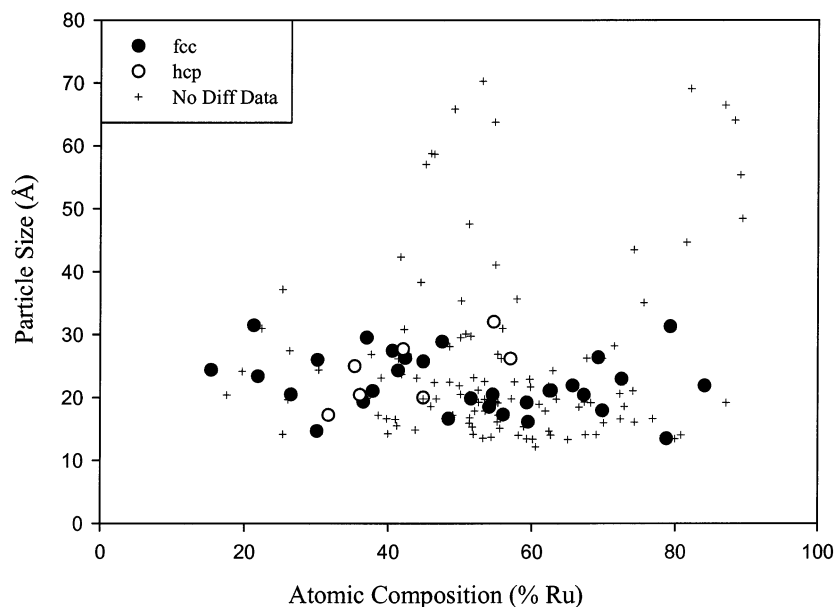


Figure 10. Phase diagram of bimetallic particles formed from the co-reduction of VXC + RuCl_3 + H_2PtCl_6 at 673 K.

this method for a 1:1 formal composition at a 20% weight loading contained a significant number of large clusters. The size and composition distributions for this system are shown in Figure 10. Particles are seen across a broad compositional range from 10% to 90% Ru. The size distribution is centered around 25 Å; however, prominent examples of large particles (>50 Å) were found to exist at both equal Pt/Ru percentages as well as extremely Ru-rich compositions. No large particles were seen where the composition was Pt-rich. To provide a comparison with the data presented in Figure 9, we measured electron microdiffraction data for a representative sampling of these clusters with sizes lying near ~ 2 nm. These are highlighted in the data presented in Figure 10. As the data suggest, the Pt-(fcc) structure again clearly dominated the apparent phase

diagram; however, the few hcp particles present had compositions that projected well into the bulk Pt(fcc) region. It thus appears that no clear bulk-like fcc/hcp phase boundary exists for bimetallic nanoparticles with sizes of a few nanometers. The data, when taken together, suggest that metastable structures can be obtained but that, on average, particles with fcc habits tend to dominate the product distribution.

Discussion

As has been shown previously, the synthesis of supported metal nanoparticles can be accomplished rather simply by the incorporation of inorganic precursors on carbon supports, followed by a reduction in H_2 at elevated temperatures.^{2,19–21} The structural properties of the products obtained can be complex,

however. In this report, we describe related procedures for the synthesis of bimetallic nanoparticles from two Pt precursors ($(\text{CH}_3)_2\text{Pt}(\text{COD})$ and H_2PtCl_6) and one Ru precursor (RuCl_3) with two different carbon supports (VXC and SAB) bearing preformed supported clusters as agents for nucleating the growth of the alloy phases (Scheme 1). In the following discussion we consider how these choices influence the size and composition distributions, as well as the ultimate structures of the nanoparticles obtained. We ultimately correlate all three factors via the construction of an apparent binary nanophase diagram for the supported bimetallic (Pt–Ru) nanoparticles. We start first with a consideration of the growth chemistries.

X-ray photoelectron spectroscopy (XPS) is a useful tool to follow the reduction process with, since it directly probes the electronic structure of the metal species present. In the monometallic precursor species, the core-level binding energies of both the unreduced Pt and Ru are shifted to higher values, consistent with the lower degree of screening of the core hole present in such species relative to a metallic state.³² The reduction leads to binding energy shifts with final values consistent with the formation of metallic ensembles (Figure 1). The microscopy fully supports this conclusion. The halogen ligands of the Cl-containing precursors, H_2PtCl_6 and RuCl_3 , are not retained on the support during the growth. The Cl-2p core level signal is completely removed by the reduction process. Taken together, the data suggest that the species formed in the alloy clusters are metallic in nature. The only interactions present in these samples, except for those occurring with metal neighbors, are ones involving the carbon support. These interactions are sufficient to prevent agglomeration of the particles beyond the limiting $\sim 2\text{--}5$ nm sizes considered in this work across the range of temperatures studied ($T \leq 823$ K).

The carbon supports do appear to influence the growth properties of homometallic clusters, albeit in ways that remain incompletely understood mechanistically. SAB samples typically gave larger particles as compared to the VXC-supported samples. Another intriguing feature is the difference in the seeded reductions of the two Pt precursors. The $(\text{CH}_3)_2\text{Pt}(\text{COD})$ precursor spontaneously nucleates cluster growth at room temperature, as evidenced by the presence of a reduced Pt(0) species in the sample prior to a H_2 exposure. For the case of the unreduced H_2PtCl_6 sample, this low temperature decomposition on the support is not observed (Figure 1C). These differences, ones related to both the character of the support and metal reagent, lead to structures that must ultimately serve to influence the patterns seen in the product distributions of the binary phases. It was for these reasons, and with the hope of simplifying the product distributions obtained, that we first employed extant clusters as nucleation centers. This substitution does in fact help to limit the size distribution of the particles formed (they tend to give far fewer anomalously large clusters at a given total weight loading, see below). Since large clusters would contain a significant fraction of the metal atoms present, this is a factor which does in fact strongly impact the weight-averaged character of the product distributions. The nucleating clusters' effects on narrowing the distributions of composition, while evident for the Pt:Ru system, are less pronounced in our hands than those seen with binary molecular cluster precursors.^{19–21} We have shown that the latter can in fact be used to prepare supported bimetallic nanoparticles with exceptionally narrow distributions of size and composition.

It is useful to consider the points related to the nature of the particle growth mechanism(s) in somewhat more detail. The

homometallic data provided in the Supporting Information clearly illustrate a significant sensitivity of the promoted growth of supported clusters to the nature of the precursor used. This is most pronounced in the contrasts seen in the structures obtained for the Ru and either of the Pt precursors. Neglecting for a moment the subtle roles played by the choice of the support, the growth of the Ru and Pt clusters follows qualitatively similar pathways. The reactions for each are carried out in a high purity hydrogen atmosphere. The conversion of the precursors in each case follows a mechanism involving a reductive condensation of species derived from the reactions of the metal reagents in this reducing atmosphere. These reactions proceed thermally under the control of a thermal ramp run to a common limiting temperature (673 K). What is not revealed by the data, however, are the temperatures at which the particle growth commences for each precursor. The final structural states of the samples do provide some qualitative insights into the nucleation dynamics that must operate for each, however. We interpret these data as suggesting that the growth is harder to initiate for the Ru clusters than it is for either of the Pt-based chemistries.

Our past experiences suggest that Pt complexes in supported form are very easy to activate/reduce (and actually may proceed spontaneously for the one precursor examined here).^{19–21} The more highly activated nature of this process for Ru is reflected in the cluster structural habits. We infer that the latter reaction leads to the formation of fewer active nuclei around which an auto-catalytic growth can be initiated. The lower number of initiation events, for a given loading of precursor, correlates directly with the larger average particle sizes obtained. This mechanism (for reasons we detail below) seems more likely to us than would having the larger sizes of the clusters result as a consequence of a higher degree of thermally induced coarsening of initial growth domains. These supported materials, in the metallic state at least, showed no tendency to progressively agglomerate at the temperatures used here.

By this line of reasoning, the Pt growth chemistries proceed via processes in which the reactive nuclei that auto-catalytically initiate the growth arise more frequently. Presumably this is due to the nucleation step being a more weakly activated process for Pt than it was for the Ru reduction. The cluster size differences seen between the H_2PtCl_6 and $(\text{CH}_3)_2\text{Pt}(\text{COD})$ derived samples must also arise as a result of the less dramatically differentiated kinetic control imposed by the dynamics of this activated process.

The formation of alloy clusters is likely to follow a mechanism closely related to that followed in the growth of the supported homometallic nanoparticles. These reactions generate a mixture of habits that result from an auto-catalytic growth mechanism. The key feature of this mechanism is the fact that the activated nucleation step generates species that are chemically amplified as precursor-derived species attach to and ultimately incorporate themselves into growing clusters. When the activation steps are kinetically very heterogeneous, then the limiting structures obtained from them will likely be so as well. It was our desire to decouple the activated initiation steps from the growth processes (as suggested by this mechanistic model) that led us to examine the possibility of using a preformed homometallic cluster to mediate the growth of the alloy phase. The clusters present on the promoted support phase would hopefully serve to template a better-controlled auto-catalytic growth process. In point of fact, the data suggest that this approach does tend to narrow the breadth of the size distribution obtained to some degree. This is most clearly established by an

inspection of the data shown in Figures 4 and 6. It is notable that these trends are evidenced in a qualitatively similar way for both the Pt on Ru/C and Ru on Pt/C depositions. At first glance, though, the distributions of composition for these samples (Figure 8) do not appear to be at all narrow. The data suggest that clusters of essentially every composition are present in the product ensemble. Some caution is warranted here. A proper analysis must in fact account for the weighting of the various cluster compositions by their size. It is essential then that the comparisons be made in ways that consider composition in terms of its real atomic distribution of mass—a strictly size-sensitive analysis. The growth of the Ru on Pt/C particles provides an instructive example in this regard.

An unpromoted growth of a Ru/Pt alloy generally gives a complex product distribution. Though numerous small particles can be formed, it still remains that a significant fraction of the sample may in fact be present in the form of a few large, poorly alloyed clusters. These large clusters can have a significant impact on a characterization of the sample in terms of its atomic distribution of mass. The promoted alloy synthesis method, especially for the reactions using RuCl_3 , decreases the number of large clusters that are formed. The data defined by the summary shown in Figure 8A illustrates the impact realized on the breadth of the distribution. As is evident in these data, though, the growth still diverges on a cluster number average basis from the limiting 1:1 stoichiometry imposed by the reagent mass balance. The sample does in fact still contain some large, poorly alloyed clusters (albeit few in number). It remains unclear to us whether the mass present in those clusters would completely explain the skewed nature of the distribution seen in this latter data set. Additional experiments will be needed to resolve this issue.

Taken together, the data suggest that the cluster-promoted growth strategy is not a perfect control strategy for mediating alloy growth in the Pt/Ru system. Regardless of initial metal loadings, the particle compositions formed after reduction are highly heterogeneous. It is possible that the observed heterogeneity is a result of a varied chemical activity of the supported monometal particles used to seed the reduction. It is not clear what the source of this varied chemical activity would be due to (if present at all), given that the presupported particles have a relatively narrow size distribution (Figures 4A and 6A). The environments contributed by the support, however, are likely to be highly heterogeneous. For example, the particles could form in regions that influence their crystallographic texture or mediate the transport properties of species derived from the precursors. One could envision, in this latter regard, that the presupported particles' relative 3D distribution could affect the binary phases final composition since neighboring particles would have to compete for precursor materials in their local environments; the growth of isolated particles would not be limited by an analogous depletion-limited mass transport of the binary precursor. These scenarios can and most likely do occur during particle growth, but the extent to which they determine the final particle's composition remains undetermined and requires further study. Regardless, the materials obtained could prove useful for research on DMFCs, especially for studies that seek to establish understandings of the rate structure sensitivities that characterize the mechanisms of anode catalysis.^{10,13} They also enable a unique opportunity to address fundamental questions related to the phase dynamics exhibited by nanoscale material systems more generally. In the section that follows, we take advantage of this opportunity and explore the influences of kinetic and thermodynamic effects on the structural dynamics

seen for the supported Pt/Ru alloys. We perform this analysis on a single-particle basis, assembling a statistical ensemble of nanoparticles that broadly explores the phase space of the system in this interesting limit.

Constructing a Binary Nanophase Diagram. We start by briefly discussing the basis of the experiment that underlies the data shown in Figure 9. Electron microdiffraction is well suited for determining the atomic scale structures of nanomaterials with limiting sizes of ~ 1 nm or larger.^{24–28} In the current work, our interest centers on the discrimination of the close-packed habits that characterize the structures adopted by extremely small metal alloy clusters. The difference between a Pt-like fcc structure and a Ru-like hcp one is subtle, lying in the stacking of planes within the lattice. In fcc structures, the hexagonal layers tile as a repeating ABC motif, whereas a hcp structure exhibits an AB stacking.³³ These stacking differences are easily differentiated via the nature of their diffraction patterns, with the caveat that a nanoscale system must be large enough to properly reflect the character of the structure. In principle, this minimum size would be an ensemble of at least 3 planes for the fcc structure (although specific reflections would likely be very weak at this limit). In this study, the clusters examined were generally of the order of 2 nm in diameter or larger, and thus large enough to fully differentiate hcp from fcc structures by electron diffraction analysis.

The data presented in Figures 9 and 10 correlate the atomic structures of the heterometallic nanoparticles with their size and composition. This correlation is presented in a form reminiscent of a binary phase diagram (here substituting size for temperature). The bulk phase diagram of the Pt/Ru binary system is well understood—only alloy phases are known to exist in the solid-phase region of the diagram.²³ At atomic concentrations of less than 62% Ru, the system adopts a Pt-like fcc structure.²³ At concentrations of greater than 80% Ru, a hcp structure is obtained.²³ A miscibility gap is found in the regions lying between these two limiting values; materials with compositions in this range exhibit coexistent phases.

There are reasons to expect that a nanoscale alloy might show structural differences from the predictions embedded in a bulk phase diagram.^{2,7,14,15,22} In the Pt/Ru system, it is now well understood that the Pt is surface active.^{2,19–21} The segregation of Pt to the surface of a cluster could shift the composition of its core to a degree that could lead to significant changes in its equilibrium phase behavior. Beyond this, though, lie the large effects that must result from the significant energies associated with the bonding of the atoms present at the surface of the cluster. For nanoscale clusters, these energies can comprise a large fraction of the total energy of the system.^{2,7,22} Together with the support interactions,²¹ these effects could come to dominate the equilibrium structural phase behaviors seen in the system.

The data for the samples grown at 673 K (Figure 9) show that particles of both fcc and hcp structures are formed. Notably, structures of both types are found in the region of the miscibility gap. The apparent phase boundaries, however, do not rigidly follow those of the bulk and many likely examples of metastable phase coexistence are evidenced. For example, fcc structures appear at concentrations as high as 90% Ru, while hcp structures appear at compositions as low as 17% Ru. Both of these structures are inconsistent with the known bulk equilibrium phase properties.²³ The dominant trend seen, though, is one of a distinct preference for the formation of fcc structures (Figure 9D). There are many more examples of fcc structures residing in either the gap or hcp domains than is true of the inverse.

The effects of particle size (in this limiting range) are much less significant. We note that we saw no evidence for the smallest particles adopting any other structures (e.g., icosahedral) as has been noted in other systems.^{22,34–39}

The most striking feature of the data presented in Figure 9 is the clear illustration it gives of the relative abilities of the supported Pt and Ru clusters to act as a template for the alloy growth. When supported Ru/C particles are used as a “substrate”, little structural memory of the bias toward hcp habits is retained. In fact, fcc nanoparticles are present whose compositions reach as high as 90% Ru. Deposition of Ru on a Pt-cluster support proceeds very differently. As shown in Figure 9A, the fcc structure of the Pt does in fact strongly template the growth of the bimetallic alloy nanoparticles. As before, the fcc structure is found in compositions reaching as high as 90% Ru. The gap and hcp zones are strongly penetrated by clusters exhibiting fcc structures. The relative importance of the kinetic and thermodynamic effects is suggested by the experiment carried out at a higher growth temperature of 823 K. While this latter data set is not as extensive as that compiled in Figure 9, it does seem to strongly support the notion that fcc structures are strongly preferred in this size range for all but the most Ru-rich compositions.

The templating effect seen in the cluster-supported growth systems (Figure 9) is seen in the unpromoted growth systems as well (Figure 10). It is presumed that, in the mixture of inorganic complexes present, the species most easily reduced will form the initial nucleating sites for particle growth. This may explain the overwhelming abundance of Pt (fcc) clusters present, but it does not account for the several (hcp) particles seen well into the bulk Pt (fcc) region. One would suspect, on the basis of the operation of an activated nucleation mechanism, that a system of mixed precursors should resemble the Ru:Pt/C samples: the relatively low energy reduction of Pt forms initial nucleation sites followed by an incorporation of Ru during growth. Given that a few (hcp) particles are seen in the gap and fcc zones, the sample seems to be more accurately approximated by a system between the two extremes examined; the majority of nucleating sites are Pt, but Ru-rich nucleation centers are still present. The size distributions, though, are sufficiently complex that we hesitate to draw larger inferences from the data beyond these suggestions.

The individual clusters studied here are too small to show phase coexistence. Clearly the idea of a miscibility gap is something that cannot project down to this limiting length scale. Rather, this property is one that must emerge at much larger particle sizes. For clusters with this composition, the fcc habit appears to be the most stable structure. Even so, the metastable states we see appear to be deeply quenched given that temperatures approaching 823 K are needed to even incompletely anneal them. This seems to be a surprisingly high temperature to us, and it may well be that, in this regard, the support interactions may in fact be playing a very significant role. Further work will be needed to clarify this point.

We close with a few final observations for future work. We have shown that supported bimetallic Pt:Ru nanoparticles can be synthesized via this seeded condensation method, and characterized these materials with several different techniques. What remains to be seen is how these structural details might be correlated with real world performances of DMFCs. Studies have shown that certain crystal faces of Pt:Ru electrodes, for example, are more electrochemically active than others.^{40,41} Considering the highly varied compositional distribution of the present growth scheme, electrochemically

active sites would also theoretically be quite structurally heterogeneous. Future work is envisioned which would seek to include studies of the electrochemical responses and thus establish the potential of these materials for applications in DMFC technology.^{42–45}

Acknowledgment. This work was supported by the Department of Energy through the Seitz Materials Research Laboratory (DEFG02-91-ER45439) and the National Science Foundation (CHE0097096). We would also like to add a special thanks to Dr. Ray Twisten for his help in gathering and analyzing our microscopy and diffraction data.

Supporting Information Available: Representative XPS spectra of materials derived from the reduction of (CH₃)₂Pt(COD), RuCl₃, and ruthenium nucleated platinum complex reductions are included. Representative TEM images and corresponding particle size distributions of the monometallic particles, indexed bimetallic nanoparticle diffraction patterns, and the elevated temperature nanoparticle phase diagram are included as well. This material is available free of charge via the Internet at <http://pubs.acs.org>.

References and Notes

- (1) Aiken, J. D.; Finke, R. G. *J. Mol. Catal. A—Chem.* **1999**, 145.
- (2) Bradley, J. S. *The Chemistry of Transition Metal Colloids*; VCH: Weinheim, 1994.
- (3) Edelstein, A. S.; Cammarata, R. C. *Nanomaterials: Synthesis, Properties and Applications*; Institute of Physics Publishing: Bristol, 1998.
- (4) Johnson, B. F. G. *Coord. Chem. Rev.* **1999**, 192, 1269.
- (5) Jortner, Z. *J. Physica D* **1992**, 24, 247.
- (6) Murray, C. B.; Kagan, C. R.; Bawendi, M. G. *Annu. Rev. Mater. Sci.* **2000**, 30, 545.
- (7) Rao, R. C. N.; Giridhar, U.; Thomas, P. J.; Edwards, P. P. *Chem. Soc. Rev.* **2000**, 29, 27.
- (8) Sinfelt, J. H. *Bimetallic Catalysts—Discoveries, Concepts, and Applications*; Wiley: New York, 1983.
- (9) Toshima, N.; Yonezawa, T. *New J. Chem.* **1998**, 22, 1179.
- (10) Landgrebe, A. R.; Sen, R. K.; Wheeler, D. J. *Proceedings of the Workshop on Direct Methanol-Air Fuel Cells* **1992**, 92–14.
- (11) Gasteiger, H. A.; Markovic, N.; Ross, P. N., Jr.; Cairns, E. J. *J. Phys. Chem.* **1993**, 97, 12020.
- (12) Gasteiger, H. A.; Markovic, N.; Ross, P. N., Jr.; Cairns, E. J. *J. Electrochem. Soc.* **1994**, 141, 1795.
- (13) Gottesfeld, S.; Zawodzinski, T. A. *Polymer Electrolyte Fuel Cells*; Wiley-VCH: Weinheim, 1997; Vol. 5.
- (14) Pan, C.; Fabrice, D.; Casanove, M. J.; Philippot, K.; Amiens, C.; Lecante, P.; Mosset, A.; Chaudret, B. *J. Phys. Chem. B* **1999**, 103, 10098.
- (15) Bruinsma, R.; Zangwill, A. *Phys. Rev. Lett.* **1985**, 55, 214.
- (16) Bubendorff, J. L.; Meny, C.; Beaurepaire, E.; Panissod, P.; Bucher, J. P. *Eur. Phys. J. B* **2000**, 17, 635.
- (17) Tadaki, T.; Koreeda, A.; Nakata, Y.; Kinoshita, T. *Surf. Rev. Lett.* **1996**, 3, 65.
- (18) Iwasita, T.; Nart, F. C.; Vielstich, W. *Ber. Bunsen-Ges. Phys. Chem.* **1990**, 94, 1030.
- (19) Nashner, M. S.; Frenkel, A. I.; Adler, D. A.; Shapley, J. R.; Nuzzo, R. G. *J. Am. Chem. Soc.* **1997**, 119, 7760.
- (20) Nashner, M. S.; Frenkel, A. I.; Somerville, D.; Hills, C. W.; Shapley, J. R.; Nuzzo, R. G. *J. Am. Chem. Soc.* **1998**, 120, 8093.
- (21) Hills, C. W.; Nashner, M. S.; Frenkel, A. I.; Shapley, J. R.; Nuzzo, R. G. *Langmuir* **1999**, 15, 690.
- (22) Freeman, D. L.; Doll, J. D. *Annu. Rev. Phys. Chem.* **1996**, 47, 43.
- (23) Hutchinson, J. M. *Platinum Met. Rev.* **1972**, 16, 88.
- (24) Cowley, J. M. *J. Electron Microsc. Tech.* **1986**, 3, 25.
- (25) Cowley, J. M.; Plano, R. J. *J. Catal.* **1987**, 108, 199.
- (26) Cowley, J. M.; Ou, H. J. *J. Electron Microsc. Tech.* **1989**, 11, 143.
- (27) Cowley, J. M. *J. Electron Microsc.* **1996**, 45, 3.
- (28) Cowley, J. M. *Microsc. Res. Tech.* **1999**, 46, 75.
- (29) Edington, J. W. *Practical Electron Microscopy*; Philips: Eindhoven, The Netherlands, 1975.
- (30) Gallezot, P.; Leclercq, C. *Characterization of Catalysts by Conventional and Analytical Electron Microscopy*; Plenum: New York, 1994.

- (31) Chescioe, D.; Goodhew, P. J. *The Operation of Transmission and Scanning Electron Microscopes*; Oxford University Press: Oxford, 1990.
- (32) Moulder, J. F.; Stickle, W. F.; Sobol, P. E.; Bomben, K. D. *Handbook of X-ray Photoelectron Spectroscopy*; Perkin-Elmer Corporation Physical Electronics Division: Eden Prairie, MN, 1992.
- (33) Shriver, D. F.; Atkins, P.; Langford, C. H. *Inorganic Chemistry*, 2nd ed.; W. H. Freeman and Company: New York, 1994.
- (34) Montejano-Carrizales, J. M.; Moran-Lopez, J. L. *Nanostruct. Mater.* **1992**, 1, 397.
- (35) Montejano-Carrizales, J. M.; Aguilera-Granja, F.; Moran-Lopez, J. L. *Nanostruct. Mater.* **1997**, 8, 269.
- (36) Vogel, W.; Rosner, B.; Tesche, B. *J. Phys. Chem.* **1993**, 97, 11611.
- (37) Hoare, M. R.; Pal, P. *Adv. Phys.* **1971**, 20, 161.
- (38) Redfield, A. C.; Zangwill, A. *Phys. Rev. Lett.* **1987**, 58, 2322.
- (39) Rodriguez, A.; Amiens, C.; Chaudret, B.; Casanove, M. J.; Lecante, P.; Bradley, J. S. *Chem. Mater.* **1996**, 8, 1978.
- (40) Waszczuk, P.; Lu, G. Q.; Wieckowski, A.; Lu, C.; Rice, C.; Masel, R. I. *Electrochim. Acta* **2002**, 47, 3637–3652.
- (41) Wasmus, S.; Kuver, A. *J. Electroanal. Chem.* **1999**, 461, 14–31.
- (42) Lizcano-Valbuena, W. H.; Paganin, V. A.; Gonzalez, E. R. *Electrochim. Acta* **2002**, 47, 3715–3722.
- (43) Arico, A. S.; Antonucci, P. L.; Modica, E.; Baglio, V.; Kim, H.; Antonucci, V. *Electrochim. Acta* **2002**, 47, 3723–3732.
- (44) Lee, S.; Park, K.; Choi, J.; Kwon, B.; Sung, Y. *J. Electrochem. Soc.* **2002**, 149, A1299.
- (45) Dinh, H. N.; Ren, X.; Garzon, F. H.; Zelenay, P.; Gottesfeld, S. *J. Electroanal. Chem.* **2000**, 491, 222–233.